TOMOGRAPHY® RESEARCH ARTICLE

Bloch–Siegert B_1-Mapping Improves Accuracy and Precision of Longitudinal Relaxation Measurements in the Breast at 3 T

Jennifer G. Whisenant[1,2], Richard D. Dortch[1,2,3], William Grissom[1,2,3], Hakmook Kang[4], Lori R. Arlinghaus[1,2], and Thomas E. Yankeelov[5]

[1]Department of Radiology and Radiological Sciences, Vanderbilt University, Nashville, Tennessee; [2]Vanderbilt University Institute of Imaging Science, Vanderbilt University, Nashville, Tennessee; [3]Department of Biomedical Engineering, Vanderbilt University, Nashville, Tennessee; [4]Department of Biostatistics and Center for Quantitative Sciences, Vanderbilt University, Nashville, Tennessee; and [5]Institute for Computational and Engineering Sciences, and the Departments of Biomedical Engineering and Internal Medicine, The University of Texas at Austin, Austin, Texas

Corresponding Author:
Thomas E. Yankeelov, PhD
Department of Biomedical Engineering,
The University of Texas at Austin,
107 West Dean Keeton Street Stop C0800, Austin, Texas 78712;
E-mail: thomas.yankeelov@utexas.edu

Key Words: T_1 mapping, quantitative breast MRI, relaxometry

Abbreviations: Variable flip angle (VFA), magnetic resonance imaging (MRI), dynamic contrast-enhanced magnetic resonance imaging (DCE-MRI), longitudinal relaxation time (T_1), repetition time (TR), repetition time (TR), inversion recovery (IR), spoiled gradient echo (SPGE), 3-dimensional (3D), echo time (TE), field of view (FOV), turbo-spin echo (TSE), fibroglandular tissue (FGT), region of interest (ROI), adipose tissue (AT), percent error (%err), concordance correlation coefficient (CCC), confidence interval (CI), coefficient of variation (CV)

ABSTRACT

Variable flip angle (VFA) sequences are a popular method of calculating T_1 values, which are required in a quantitative analysis of dynamic contrast-enhanced (DCE) magnetic resonance imaging (MRI). B_1 inhomogeneities are substantial in the breast at 3 T, and these errors negatively impact the accuracy of the VFA approach, thus leading to large errors in the DCE-MRI parameters that could limit clinical adoption of the technique. This study evaluated the ability of Bloch–Siegert B_1 mapping to improve the accuracy and precision of VFA-derived T_1 measurements in the breast. Test–retest MRI sessions were performed on 16 women with no history of breast disease. T_1 was calculated using the VFA sequence, and B_1 field variations were measured using the Bloch–Siegert methodology. As a gold standard, inversion recovery (IR) measurements of T_1 were performed. Fibroglandular tissue and adipose tissue from each breast were segmented using the IR images, and the mean T_1 was calculated for each tissue. Accuracy was evaluated by percent error (%err). Reproducibility was assessed via the 95% confidence interval (CI) of the mean difference and repeatability coefficient (r). After B_1 correction, %err significantly ($P < .001$) decreased from 17% to 8.6%, and the 95% CI and r decreased from ±94 to ±38 milliseconds and from 276 to 111 milliseconds, respectively. Similar accuracy and reproducibility results were observed in the adipose tissue of the right breast and in both tissues of the left breast. Our data show that Bloch–Siegert B_1 mapping improves accuracy and precision of VFA-derived T_1 measurements in the breast.

INTRODUCTION

Dynamic contrast-enhanced magnetic resonance imaging (DCE-MRI) is a common method for evaluating tumor response to therapy in a variety of cancers (1-3), including breast (4, 5). DCE-MRI acquires images before, during, and after injection of a contrast agent to characterize, for example, tumor-related perfusion. To perform a quantitative analysis of DCE-MRI data, knowledge of the precontrast longitudinal relaxation time (T_1) is required to convert the measured dynamic signal intensity into a time course of the concentration of the contrast agent (6). A popular technique used to measure the precontrast T_1 is the variable flip angle (VFA) approach, which uses a series of spoiled gradient echo (SPGE) images acquired with a short, fixed repetition time (TR) and a varying flip angle (7, 8). The resulting data are then fit to the signal intensity equation describing the SPGE acquisition with T_1 as a fit parameter for each voxel or region of interest (ROI). Although this technique allows for rapid 3-dimensional (3D) T_1 mapping, it is not without limitations, chief of which is that its accuracy is dependent on the uniformity of the transmit radiofrequency (B_1) field. It should be noted that other T_1 mapping methods exist that are less sensitive to variations in the transmit field (9); however, VFA sequences are the preferred method in the clinical setting, as these acquisitions enable a large field of view (FOV) to be measured in a relatively short period.

Inhomogeneities in the B_1 field cause variations in the prescribed flip angles, leading to inaccurate measurements of T_1, which can subsequently induce large errors in the DCE-MRI

ISSN 2379-1381 http://dx.doi.org/10.18383/j.tom.2016.00133

parameters (eg, the volume transfer rate constant, K^{trans}) (10). Indeed, simulation results indicated that errors in K^{trans} ranged from 15% to 500% as the error in the T_1 measurement ranged from 14% to 65% of the nominal value (11). Therefore, an inaccurate estimation of the precontrast T_1 could potentially lower the sensitivity of DCE-MRI for characterizing tumor vascular properties, thereby limiting the utility of the technique.

The B_1 field experienced by spins within the body is influenced by several factors, including the distance of the spins from the radiofrequency transmit coil, the dielectric properties of the tissues, and the factors related to body size and wavelength of the radiofrequency (12). The severity of the nonuniformity in the B_1 field increases at higher field strengths (13), and noticeable B_1 inhomogeneities have been observed in the breast at 3 T (14-17). In particular, a substantial variation in the B_1 field from left to right across the imaging FOV has been observed, which may artificially decrease the contrast enhancement in specific lesions (18). Thus, Kuhl et al. have suggested that B_1 mapping in the breast should be a standard practice (14). Although several different methods for B_1 mapping have been developed (12, 19-22), no single method has emerged for widespread application.

A technique using the Bloch–Siegert shift to map the B_1 field has recently been developed, and it is an area of active investigation (23-26). The Bloch–Siegert shift is a term used to describe the shift in resonance frequency of a nucleus when an off-resonance radiofrequency field is applied (27). Although Sacolick et al. (24) provide the details, the salient information is mentioned here. If a radiofrequency pulse is applied either far enough off-resonance and/or with a pulse shape such that it does not cause spin excitation, the spins experience a change in precession frequency without excitation (28). The spin precession frequency shifts away from the off-resonance irradiation and is dependent on the magnitude of the B_1 field, as well as the difference between the spin resonance frequency and radiofrequency field. The shift in frequency results in a phase shift in the images that can be used to spatially map the B_1 magnitude. This phase-based method generates a B_1 map that is not significantly biased by TR, T_1 relaxation, flip angle, chemical shift, background field inhomogeneity, or magnetization transfer (24). The insensitivity to TR is especially important in a clinical setting, as it allows for the prompt acquisition of image data with a short TR. In the current study, we present an approach to rapidly, accurately, and precisely map B_1 and T_1 values in the breast using the Bloch–Siegert method with a VFA sequence.

METHODOLOGY

All imaging data were acquired with a 3 T Achieva magnetic resonance scanner (Philips Healthcare, Best, The Netherlands) equipped with a 2-channel multitransmit body coil and a MammoTrak table including a 16-channel receive double-breast coil (Philips Healthcare, Best, The Netherlands).

Phantom Scans

To investigate the feasibility of the approach, 8 gel phantoms (The Eurospin II Test System, Diagnostic Sonar, Livingston, Scotland, UK) submerged in water were scanned at room temperature. The T_1 values of the phantoms ranged from 300 to 1600 milliseconds. A coronal image volume was placed in the center of the breast coil containing the phantoms, and VFA, Bloch–Siegert, and inversion recovery (IR) data were collected. VFA data with 10 flip angles (2, 4, 6, . . . 20) were acquired using a 3D SPGE sequence with the following parameters: TR/echo time (TE) = 7.9/4.6 milliseconds, sensitivity encoding parallel imaging factor of 2, acquisition matrix of 192 × 192 over a FOV of 256 × 256 mm^2, yielding a voxel size of 1.33 × 1.33 mm^2, and 15 slices with a thickness of 4 mm for a total scan time of 66 seconds. The Bloch–Siegert data were collected using a gradient echo sequence with a 2-millisecond frequency-swept B_1 phase imparting pulse (25) over the same FOV as the VFA data with the following parameters: TR/TE = 491/5.4 millisecond, acquisition matrix of 104 × 102, reconstruction voxel size of 1.33 × 1.33 mm^2, and root mean square B_1 field = 2.29 μT for a total scan time of 104 seconds. As is required with the Bloch–Siegert B_1 mapping, 2 images were collected at opposite frequency offsets. As a gold standard, a 2-dimensional IR-prepared turbo-spin echo (IR-TSE) sequence was used to acquire a single slice corresponding to the center of the VFA image volume with the following parameters: 12 inversion times of 25, 50, 75, 100, 200, 300, 400, 500, 1000, 2000, 4000, and 10 000 milliseconds, acquisition matrix of 128 × 96 over an FOV of 256 × 256 mm^2, reconstruction voxel size of 1.33 × 1.33 mm^2, predelay before inversion pulse of 2500 milliseconds, and TSE factor of 24 with an echo spacing of 5.9 milliseconds for a total scan time of 125 seconds.

Subject Scans

Test–retest MRI sessions were performed on 16 women (median: 42 years, range: 25–67) with no history of breast disease. Because of age, body habitus, or hormonal status, 4 of these women did not have appreciable fibroglandular tissue (FGT) in either breast; thus, measurements for these women included data only from the adipose tissue (AT). The imaging protocol consisted of 2 scan sessions each lasting ~30 minutes separated by a 10-minute rest period. During the rest period, the subjects were removed from the scanner and allowed to stretch. All subjects were consented as part of an ongoing study approved by the local Institutional Review Board.

For each test–retest session, 2 separate sagittal imaging volumes were centered on each breast with an attempt to approximately match the stack placement between each imaging session. Subsequent VFA, Bloch–Siegert, and IR data were then collected separately for each breast. The imaging parameters for each sequence were identical to the phantom scans, except that the slice thickness was 5 mm and the number of slices for the VFA and Bloch–Siegert sequences was 10. These 2 parameters were changed to match our ongoing clinical imaging trial (29). In addition, we applied the T_1 and Bloch–Siegert B_1 mapping methods described herein on 3 patients with breast cancer. Each patient provided written consent to participate in the study.

Image Analysis

All image data were exported to MATLAB R2013b (The MathWorks, Natick, Massachusetts) for analysis. Bloch–Siegert B_1 maps were calculated as described previously (25). In brief, the actual flip angle at each image voxel was obtained via linear interpolation of the entries of a phase difference-versus-B_1

strength lookup table generated using Bloch equation simulations of the off-resonant Bloch–Siegert pulse. The flip angle correction map was then calculated as the ratio of the actual flip angle to the prescribed flip angle.

VFA T_1 maps with and without B_1 correction were obtained by fitting signal intensity (S) data to equation 1 as follows:

$$S = S_0 \cdot \frac{\sin(f \cdot \alpha) \cdot (1 - \exp(-TR/T_1)}{1 - (\exp(-TR/T_1) \cdot \cos(f \cdot \alpha))} \quad (1)$$

where S_0 is a constant related to scanner gain and proton density, α is the prescribed flip angle, and f is the Bloch–Siegert-derived flip angle correction factor (set to 1 for the uncorrected T_1 map), and we have taken TE $\ll T_2$*. In addition, T_1 maps were calculated by fitting the IR-TSE data (30) to equation 2 as follows:

$$S = S_0 \cdot |(\cos\alpha \cdot (1 - \exp(-TD/T_1)) \cdot \exp(-TI/T_1)) + 1 - \exp(-TI/T_1)| \cdot \quad (2)$$

For the phantom scans, circular ROIs were manually drawn within each gel phantom using the IR data as a guide. The average T_1 from each phantom was recorded from the IR T_1 map. The same ROIs were then subsequently used to calculate the average T_1 from the central slice of the VFA-derived T_1 maps with and without B_1 correction. Statistical analyses were performed on the average T_1 values calculated from each ROI. To evaluate the accuracy of the proposed B_1 mapping technique, the percent error (%err) between the IR- and VFA-derived T_1 values (with and without B_1 correction) was calculated.

For healthy volunteers, segmentation masks for AT were automatically generated from the IR data (inversion times = 500 milliseconds), where the signal intensity for the FGT was close to 0. A representative example of the segmentation masks for each tissue is presented in Supplemental Figure 3. FGT segmentation masks were subsequently generated as the opposite of the AT mask after manually segmenting the skin and chest wall from the FOV. The average T_1 from each tissue segmentation mask was recorded from the IR T_1 maps for each breast and imaging session. The same tissue masks were then used to calculate the average T_1 from the central slice of the VFA-derived T_1 maps (with and without B_1 correction). The %err between the VFA-derived T_1 values (with and without B_1 correction) and the IR T_1 values was calculated to evaluate the accuracy, and the agreement between the different T_1 values was assessed via the concordance correlation coefficient (CCC). Furthermore, the bootstrap 95% confidence interval (CI) of the mean differences in absolute deviation between IR- and VFA-derived T_1 values (with and without B_1 correction) was computed as previously described (31) using equation 3 as follows:

$$avg_i = \text{average}(|VFA\text{-}IR| - |VFA_{B_1}\text{-}IR|) \quad (3)$$

where VFA and VFA_{B_1} are VFA-derived T_1 values without and with B_1 correction, respectively. Equation 3 is first computed with all T_1 values (ie, 2 scan sessions per subject equals 32 and 26 T_1 values for AT and FGT, respectively, in each breast). Next, the $n \times m$ matrix of data is randomly resampled with replacement from the original data set (such that data from a subject(s) could be included more than once) and then equation 3 is recomputed. In the AT case, for example, the $m \times n$ matrix size is 16 × 2, as there are 16 patients with 2 data points each. This process is repeated 1000 times, generating a new matrix of $m \times n$ data points, which are then used to calculate the upper and lower bounds of the bootstrap 95% CIs. The number of data points n is the total number of subjects.

To illustrate the application of the T_1 and B_1 mapping techniques described herein, manual ROIs were drawn in the AT, FGT (if appreciable), and tumor of 3 patients with breast cancer. Average T_1 from each ROI was calculated, and the %err between the VFA-derived T_1 values (with and without B_1 correction) and the IR T_1 values was compared.

Reproducibility Statistics

Reproducibility statistics used in this test–retest study follow the methods previously described by Bland and Altman (32) and are similar to what was previously implemented in the breast of healthy volunteers (33, 34). First, the difference, d, was calculated between the 2 VFA T_1 data sets obtained for each subject and then the distribution of those differences was tested for normality using the Shapiro–Wilk test. The Kendall's Tau test was used to ensure that the magnitude of the difference values was not correlated with the parameter mean of the repeated measurements. The Wilcoxon signed-rank test was used to test the null hypothesis of no bias (ie, average difference is 0) between repeated measurements.

The statistical measurements of reproducibility were calculated as follows:

(1) The root-mean-square deviation ($rMSD$) is computed using the differences, d, as follows:

$$r\text{MSD} = \sqrt{\frac{\sum d^2}{n}}. \quad (4)$$

(2) The 95% CI for a group of n subjects is shown as follows:

$$\text{CI} = \pm \frac{1.96 \cdot \text{std}(d)}{\sqrt{n}} \quad (5)$$

where std(d) is the standard deviation of d. The confidence interval indicates the range of expected measurement variability in a group of n subjects.

(3) The within-subject standard deviation (wSD) is as follows:

$$\text{wSD} = \frac{\text{rMSD}}{\sqrt{2}} \quad (6)$$

(4) The repeatability coefficient (r) is shown as follows:

$$\text{r} = 2.77 \cdot \text{wSD} \quad (7)$$

Or, equivalently, as follows:

$$\text{r} = 1.96 \cdot \text{rMSD} \quad (8)$$

The repeatability coefficient defines the magnitude of the maximum difference expected in 95% of paired observations; for example, r defines the expected measurement variability for an individual. Because of our moderate sample sizes, we replaced 1.96 in equation 5 with the appropriate t-statistic for our

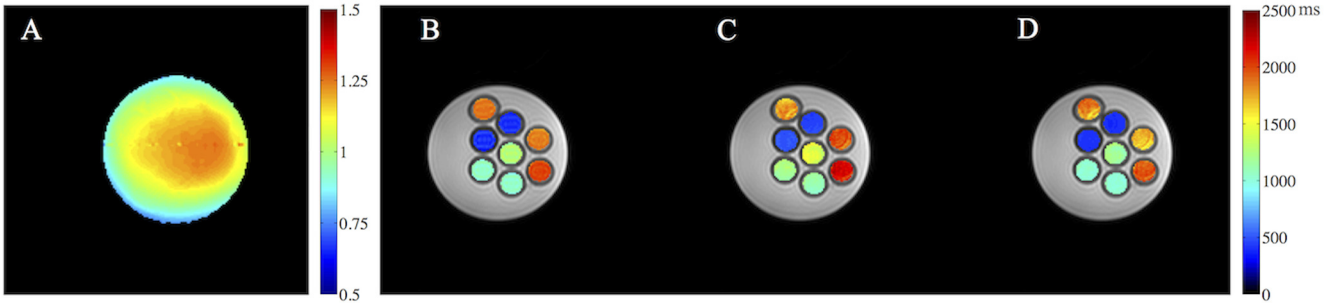

Figure 1. A Bloch–Siegert B_1 map (A) with T_1 parametric maps calculated from inversion recovery (IR) (B) and uncorrected variable flip angle (VFA) (C), and B_1-corrected VFA data (D) are shown for the gel phantoms. The Bloch–Siegert B_1 map shown is the correction factor, which is the ratio of the actual and nominal flip angles. Note the large spatial variation across the B_1 map; this variation is a representation of the B_1 inhomogeneity across the imaging field of view (FOV). After B_1 correction, the VFA-derived T_1 values (D) are more similar to the IR T_1 values (B) in each gel phantom.

sample size, which was 2.131 (n = 16) and 2.179 (n = 13) for AT and FGT, respectively.

Statistical analyses were performed using the statistical toolbox in MATLAB®. A significance value of $P \leq .05$ was used for all statistical tests. In addition, we quantified the coefficient of variation (CV) between the repeated measurements, which is the ratio of the standard deviation of the repeated measurements over the mean of the repeated measurements.

RESULTS

Gel Phantoms

A set of image data for the gel phantom experiment is displayed in Figure 1. The Bloch–Siegert B_1 map is displayed in Figure 1A, where each voxel represents the Bloch–Siegert-derived flip angle correction factor (ie, ratio of the actual flip angle to the nominal flip angle) that is incorporated into equation 1. T_1 parametric maps generated from the IR, uncorrected VFA, and B_1-corrected VFA data are displayed in panels B, C, and D, respectively, of Figure 1. The mean (±standard deviation) T_1 value for each gel phantom ROI, along with the %err from the IR data, is listed in Table 1. Compared with the uncorrected VFA data, the B_1-corrected VFA-derived T_1 estimates have a significantly lower %err ($P = .016$, Wilcoxon signed-rank).

In Vivo Scans

A representative set of image data is displayed for the right breast of 1 subject in Figure 2. (Identical data for the left breast in the same subject are displayed in Supplemental Figure 1.) The Bloch–Siegert B_1 maps from both scans are displayed in Figure 2, A and E, where each voxel displays the Bloch–Siegert-derived flip angle correction factor. Also shown, are test–retest T_1 parametric maps generated from the IR (panels B and F), uncorrected VFA (panels C and G), and B_1-corrected VFA (panels D and H) data. Average T_1 values from each tissue ROI and T_1 mapping technique are tabulated for the right and left breast from each subject in Supplemental Tables 1 and 2, respectively.

Table 2 lists the accuracy results for each ROI and breast. In the right breast, %err in the FGT using the VFA method significantly ($P < .001$, Wilcoxon signed-rank) decreased from 17.0% to 8.6% and the CCC increased from 0.55 to 0.83 after B_1 correction. Similar trends in accuracy were observed in the AT (Table 2). Bootstrap 95% CIs for FGT and AT were 57.8–139

Table 1. Average ± Standard T_1 (milliseconds) Values and %err in the Gel Phantoms

Tube No.	IR	VFA w/o B_1	%err	VFA w/B_1	%err
1	322 ± 25	364 ± 14	13	319 ± 8	1
2	328 ± 37	401 ± 10	22	331 ± 9	1
3	835 ± 37	889 ± 39	7	816 ± 20	2
4	843 ± 39	963 ± 40	14	822 ± 22	3
5	1004 ± 51	1160 ± 21	15	940 ± 43	6
6	1478 ± 54	1573 ± 59	6	1357 ± 56	8
7	1500 ± 19	1412 ± 64	6	1454 ± 87	3
8	1558 ± 22	1727 ± 62	8	1558 ± 50	3

Abbreviations: No., number; %err, percent error; IR, inversion recovery; VFA, variable flip angle.

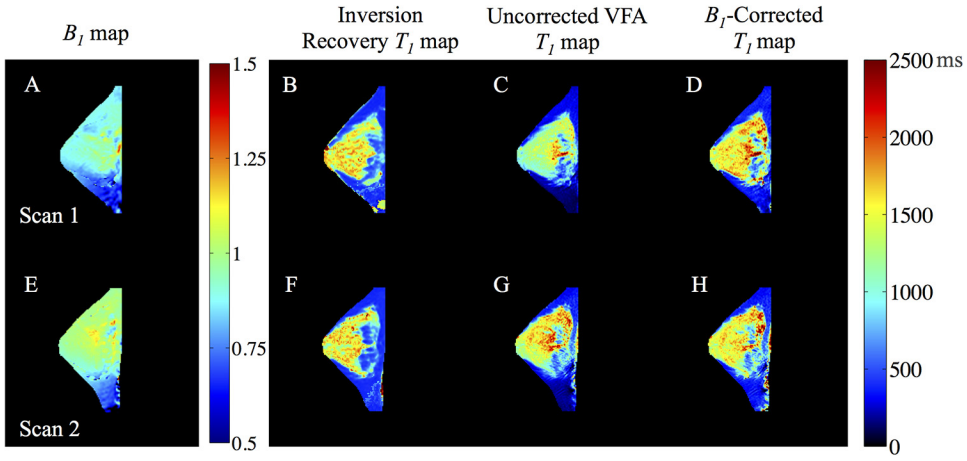

Figure 2. A representative test–retest set of B_1 and T_1 parametric maps displayed for the right breast of a healthy volunteer. Bloch–Siegert B_1 maps (A and E) correspond to the correction between the actual and the nominal flip angles. Note the spatial variation of the correction factors in the B_1 maps and the difference in B_1 maps between repeated scans; together, these images provide evidence that a B_1 map should be incorporated into routine breast imaging if a quantitative analysis of the collected data is desired. T_1 parametric maps include: IR maps (B and F), uncorrected VFA maps (C and G), and B_1-corrected VFA maps (D and H). The spatial variations in T_1 of the FGT are minimized after B_1 correction, and the T_1 map more closely matches the IR T_1 map. Furthermore, the B_1-corrected T_1 maps are visually more similar between repeated measurements compared with the uncorrected data. Observe how the orientation is slightly different between repeated scans, which might negatively affect the T_1 reproducibility, as the same tissue sections from each scan might not be analyzed.

milliseconds and 17.2–42.2 milliseconds, respectively. The range of CIs for each tissue includes all positive numbers, and by referring to equation 3, it can be seen that the absolute difference from the gold standard IR T_1 is smaller after B_1 correction for both tissue ROIs. In the left breast, %err in the FGT using the VFA method significantly ($P = .002$, Wilcoxon signed-rank) decreased from 15.0% to 8.7% and the CCC increased from 0.60 to 0.83 after B_1 correction. Similar trends in accuracy were observed in the AT (Table 2). The bootstrap 95% CIs for FGT and AT were 35.8–104.8 milliseconds and 2.4–26.7 milliseconds, respectively; again, both values for each CI were positive, indicating that the absolute difference from gold standard IR T_1 is smaller after B_1 correction for both ROIs.

Table 2. Accuracy Results for Both Breasts and ROI

	Right Breast		Left Breast	
	%err (Std)	CCC	%err	CCC
Adipose Tissue				
VFA	13% (9.7%)	0.26	13% (11%)	0.29
VFA w/B_1	6.2% (4.8%)	0.59	9.4% (7.3%)	0.5
Fibroglandular Tissue				
VFA	17% (9.1%)	0.55	15% (11%)	0.6
VFA w/B_1	8.6% (7.4%)	0.83	8.7% (5.5%)	0.83

Abbreviations: ROI, region of interest; %err, percent error; Std, standard deviation; CCC, concordance correlation coefficient; VFA, variable flip angle.

As a proof of principle, the T_1 and B_1 mapping methods were applied in 3 patients with breast cancer. Figure 3 displays T_1 parametric maps for all 3 patients generated from IR (left column), uncorrected VFA (center column), and B_1-corrected VFA (right column) data. From these images, it can be seen that the B_1-corrected T_1 values in the tumors more closely match the IR T_1 values. This similarity is extremely important, as accurate T_1 values are required when performing a quantitative DCE-MRI analysis. The mean (±standard deviation) T_1 value for each tissue ROI, along with the %err from the IR data, is listed in Table 3 for each patient with breast cancer. Compared with the uncorrected VFA data, the B_1-corrected VFA-derived T_1 estimates have, on average, a lower %err. Combining all tissue ROIs for each imaging technique, a significantly lower %err was observed after B_1 correction ($P = .004$, Wilcoxon signed-rank).

Reproducibility

Reproducibility statistics for each tissue are listed in Table 4 and Supplemental Table 3 for the right and left breast, respectively. Normality was assumed for each data set as determined by the Shapiro–Wilk test. No data sets had an average difference significantly different from 0 as determined by the Wilcoxon signed-rank test. In addition, the Kendall's Tau test showed that the difference between repeat measurements d was independent of the mean for each ROI.

Bland–Altman plots for each tissue ROI are displayed in Figure 4 and Supplemental Figure 2 for the right and left breast, respectively. Each panel displays the difference in T_1 between

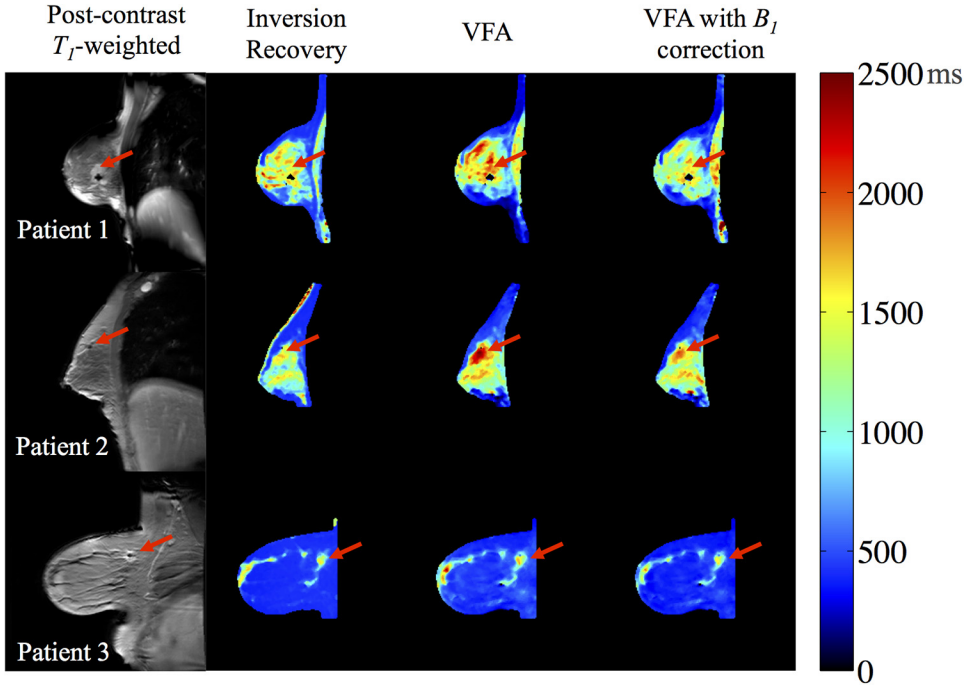

Figure 3. As a proof of principle, the B_1 and T_1 methods presented in this article were performed on 3 patients with breast cancer; each patient was a subject enrolled in our ongoing breast imaging clinical trial (29). T_1 parametric maps are shown for IR (left center column), uncorrected VFA (right center column), and B_1-corrected VFA (right column) data collected from each patient (shown in rows). The tumors are shown with red arrows in each image. Compared with the uncorrected VFA data, the B_1-corrected VFA T_1 values of the FGT, AT, and tumor in all 3 patients are more similar to the IR T_1 values, thus suggesting a more accurate T_1 value in each tissue after B_1 correction. Note that circular regions in the breasts that have a lack of signal intensity are due to the presence of a breast biopsy clip.

the repeated scans against the mean T_1 from both scans. The mean difference and 95% CIs of the mean difference are displayed as black and blue lines, respectively. The 95% CIs of the mean difference, which define expected measurement variability for a cohort of subjects, decreased after B_1 correction. For the right breast, the 95% CI of the mean difference of the AT ROI decreased from ±28 milliseconds (6.5%) to ±14 milliseconds (3.3%) after B_1 correction, whereas the 95% CI of the mean difference for the FGT ROI decreased from ±94 milliseconds (7.1%) to ±38 milliseconds (3.0%). The repeatability coefficient (red lines in Figure 4 and Supplemental Figure 2), which defines the measurement variability in an individual, decreased from 104 to 48 milliseconds in AT and from 276 to 111 milliseconds in FGT after B_1 correction. Similar trends in the 95% CI of the

Table 3. Average ± Standard T_1 (milliseconds) Values and %err from ROIs in Patients with Breast Cancer

Patient	ROI	IR	VFA w/o B_1	%err	VFA w/B_1	%err
1	Tumor	1364 ± 292	1682 ± 330	23	1514 ± 269	11
	AT	411 ± 10	470 ± 48	14	384 ± 36	7
	FGT	1391 ± 336	1807 ± 215	30	1383 ± 164	1
2	Tumor	1374 ± 376	2104 ± 267	53	1721 ± 209	25
	AT	397 ± 10	439 ± 34	11	409 ± 33	3
	FGT	1493 ± 224	1725 ± 99	16	1578 ± 79	6
3	Tumor	1101 ± 345	1275 ± 381	16	1151 ± 344	5
	AT	407 ± 7	465 ± 45	14	415 ± 41	2
	FGT	1471 ± 319	2036 ± 343	38	1594 ± 271	8

Abbreviations: ROI, region of interest; %err, percent error; IR, inversion recovery; VFA, variable flip angle; AT, adipose tissue; FGT, fibroglandular tissue.

Table 4. Reproducibility Results for the Right Breast

	Mean	Mean Difference	95% CI for Mean Difference	wSD	Repeatability	CV (Mean ± SD)
Adipose Tissue						
VFA	429	40	±28 (6.5%)	38	104	6.7% ± 6.1%
VFA w/B_1	418	19	±14 (3.3%)	18	48	3.2% ± 3.0%
Fibroglandular Tissue						
VFA	1316	106	±94 (7.1%)	100	276	4.7% ± 4.9%
VFA w/B_1	1256	49	±38 (3.0%)	40	111	2.6% ± 1.5%

Abbreviations: CI, confidence interval; wSD, within-subject standard deviation; CV, coefficient of variation; SD, standard deviation; VFA, variable flip angle.

mean difference and r were observed for both tissues in the left breast (Supplemental Table 3).

In the right breast, the CV (Table 4) significantly ($P = .039$, Wilcoxon signed-rank) decreased from 6.7% to 3.2% in the AT after B_1 correction. In the FGT, the CV decreased from 5.5% to 2.2% after B_1 correction; however, the difference was not statistically significant ($P = .064$). In the left breast (Supplemental Table 3), the CV significantly decreased from 7.5% to 3.9% in the AT ($P = .002$) and 6.8% to 2.4% in the FGT ($P = .016$) after B_1 correction.

DISCUSSION

It is well known that variations in the B_1 transmit field exist in the breast at 3 T (14, 35). Thus, applying a B_1 correction scheme is critical—especially when measuring T_1 with an acquisition technique that requires multiple flip angles (ie, the VFA technique). Any bias in the prescribed flip angle will lead to inaccuracies in the measured T_1. The observed T_1 values in the AT and FGT in this study are not unreasonable and are similar to a recent study by Bedair et al. that investigated the

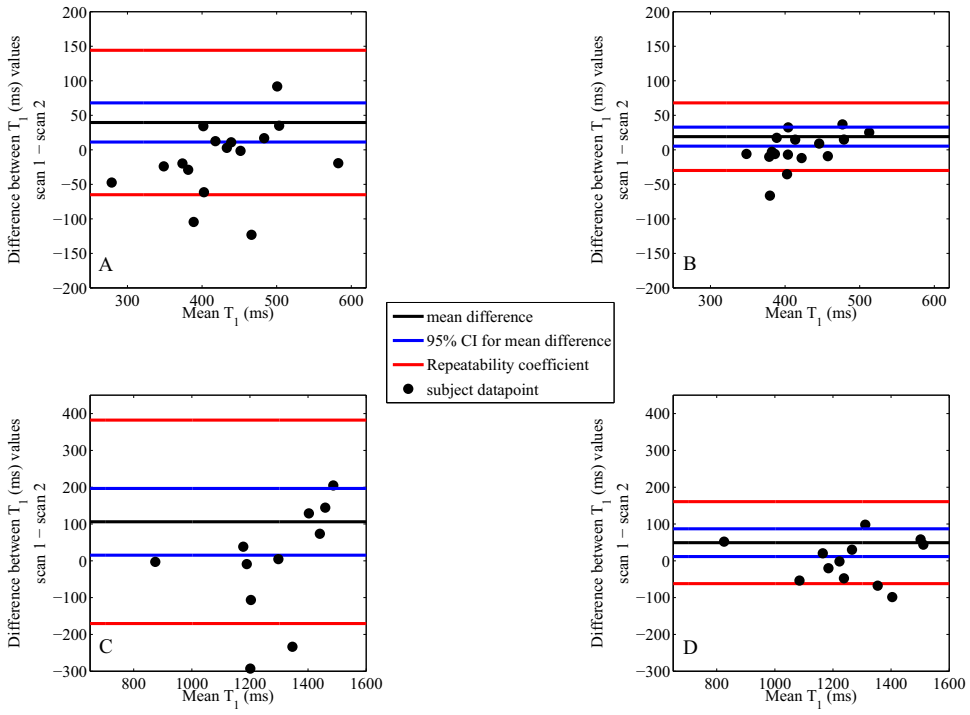

Figure 4. Bland–Altman plots for the right breast displaying the difference in T_1 between repeated measurements plotted against mean T_1 for AT before B_1 correction (A), AT after B_1 correction (B), FGT before B_1 correction (C), and FGT after B_1 correction (D). The mean difference (black line) is shown with 95% confidence intervals of the mean difference (blue lines), which defines a measure of the spontaneous variability that is expected in a cohort of subjects. Repeatability is also shown (red lines), which quantifies the maximum difference expected to be observed between 2 repeat measurements in an individual. It can be noted from the figure that the width of both the 95% CIs of the mean difference and repeatability coefficient decreases after B_1 correction, suggesting a lower variability.

effect of a Bloch–Siegert B_1 correction technique on VFA-derived measurements of T_1 in the breast at 3 T (36). In addition, our study incorporated a comparison with the gold standard IR data and a reproducibility analysis, allowing for an evaluation of accuracy and precision of the combination of the Bloch–Siegert B_1 and the VFA T_1 mapping techniques. We showed that the T_1 and B_1 mapping methods described herein are not only appropriate for clinical applications but also produce accurate estimates of T_1 in breast tissues, including FGT, AT, and breast cancer.

The feasibility of the presented T_1 and B_1 mapping techniques was shown in the gel phantom experiment. After B_1 correction, the VFA-derived T_1 values in each gel phantom more closely matched the gold standard IR T_1 values, which was supported by the significantly lower %err ($P = .016$, Wilcoxon signed-rank). In addition, we observed that the Bloch–Siegert B_1 mapping technique improved the accuracy of the VFA-derived T_1 measurements in the breast. The %err in both ROIs (ie, FGT and AT) decreased after B_1 correction for both breasts, suggesting that a smaller difference exists between the B_1-corrected VFA and IR T_1 values as compared to the uncorrected VFA data. The bootstrap 95% CIs were positive for all ROIs (including both breasts), indicating that the T_1 values after B_1 correction are more similar to the IR T_1 data. Furthermore, the CCC increased by ~50% for all measurements after B_1 correction. Although the CCC value in the AT ROIs increased after B_1 correction, the level of agreement after B_1 correction was minimal (ie, CCC = ~0.5) and much lower than the CCCs in the FGT. The radiofrequency pulses for the Bloch–Siegert technique described in this study were designed to produce pure phase shifts over a ±600 Hz range (25); however, these phase shifts will have some (albeit small) sensitivity to off-resonance effects over that range. In principle, ±600 Hz should be sufficient for AT alone, but it could be problematic if a chemical shift exists in the field gradients. This could explain the observed lower agreement, as measured by the CCC, between the B_1-corrected VFA and IR T_1 values in the AT. The potential off-resonance effects should not be considered a limitation to the Bloch–Siegert method, however, and can be compensated for using a map of the static magnetic field (ie, a B_0 map).

There have been several recent studies investigating various B_1 correction schemes for accurate T_1 mapping of the breast at 3 T. Sung et al. (35) evaluated the accuracy of T_1 measurements in the AT using the double-angle method of B_1 mapping, which is a technique that uses the signal magnitude images at nominal flip angles α and 2α. Their results showed an average relative flip angle variation of 115% on the left breast and 82% on the right breast, which improved to 7% after B_1 correction (35). Although the double-angle method generates robust measurements of B_1 inhomogeneity, it is limited by its T_1 dependence and the requirement for long TRs to mitigate the T_1 dependence, which provides a possible barrier to clinical applications. The same group developed a technique to simultaneously map B_1 and T_1 using the AT as a reference region, and compared their results to the double-angle method (17). This technique uses a 2-point Dixon algorithm (37) to generate AT-only images and then assigns a known T_1 value to a ratio of signal magnitudes to compute the B_1 field variation. Sung et al. observed that the B_1 maps generated with their postprocessing technique were similar to the double-angle method (17); therefore, they concluded that their approach, which is more time-efficient than the double-angle method, could be used to correct B_1 inhomogeneities in breast MRI data.

Pineda et al. also developed a reference region technique to map the B_1 transmit field using a population-average T_1 value in the AT that was measured using an inversion recovery spectroscopic technique (16). These investigators evaluated their B_1-mapping technique by comparing VFA-derived T_1 values (before and after B_1 correction) to IR T_1 values in the breasts of 4 patients. Before correction, the absolute difference between VFA and IR values was 58% ± 21%, which was reduced to 8.1% ± 7.8% after the B_1 correction (16). Although we observed similar results in our study, the Bloch–Siegert technique described herein is not limited by the necessary assumptions of a reference region technique, with the first assumption being that the T_1 of AT in the breast is globally uniform and well characterized (16, 17). The second is the requirement for a large section of tissue in the FOV with a homogenous T_1, which may not always be available in, for example, women with dense breasts (17). Another B_1 mapping technique that may show promise in breast imaging is the DREAM approach by Nehrke and Bornert (38), which is a novel approach for robust, ultrafast, multislice B_1 mapping.

The reproducibility analysis performed in this study provides objective statistical thresholds that define the range of repeatability by quantifying the maximum difference expected to be observed between 2 repeat measurements in an individual. In addition, the 95% CIs for the mean difference provide a measure of the spontaneous variability that is expected in a cohort of subjects. Both the 95% CIs of the mean difference and repeatability coefficient are useful when defining the associated variability in a measurement so that future studies can be designed and statistically powered appropriately. We observed lower 95% CIs of the mean difference and repeatability coefficients after B_1 correction in all ROIs (including both breasts). We also observed an ~50% reduction in the coefficient of variation between the repeated measures, thus suggesting lower variability after B_1 correction. Therefore, our reproducibility analysis showed that the Bloch–Siegert B_1 mapping technique improved reproducibility, thereby also improving precision, of VFA-derived T_1 measurements in the breast at 3 T.

We attempted to be as consistent as possible when positioning each subject in the scanner and determining the imaging FOVs between repeated acquisitions. However, image registration between repeat acquisitions was not performed because the success of the registration results would be limited by the single-slice IR acquisition. We note that this is a limitation in the current study, as tests for accuracy and reproducibility were performed using only 1 slice. We would expect, however, that applying a longitudinal registration technique (39) would only improve accuracy and precision, as differences in subject position and imaging FOV would only minimally impact the results. In addition, by using the average T_1 value from all of the AT and FGT voxels in the FOV, we felt that the accuracy and precision results would not be biased by a reader who, for example, would manually draw ROIs in the tissues. Another limitation to our study is the different number of data sets in the AT and FGT analyses. Our goal was to recruit a cohort of subjects with an age range that was representative of our ongoing clinical breast imaging study (29); however, some of the women included in this study had very little or no FGT because of either age

or body habitus. We noted above that off-resonance effects could limit the accuracy of the Bloch–Siegert approach in areas of the breast where a chemical shift exists in the field gradients, which, for example, could be in the AT and areas of the breast with a mixture of AT and FGT. This limitation, however, would only affect the accuracy results described herein and should not be considered as a limitation of the Bloch–Siegert method, as chemical shift effects can be minimized by incorporating a map of the static magnetic field into the correction scheme.

CONCLUSION

The VFA technique is often used in clinical applications of DCE-MRI, as it allows for 3D T_1 mapping in a time-efficient manner. However, the accuracy of the technique is severely affected by inhomogeneities in the B_1 transmit field, which are known to be significant in the breast at 3 T (14). The difference in the prescribed flip angle due to B_1 inhomogeneities leads to inaccuracies in VFA-derived estimates of T_1, which can compound to large errors in, for example, the DCE-MRI parameter K^{trans} (11, 36). Large errors in DCE-MRI analyses could lower the sensitivity and specificity of the imaging technique, thereby limiting clinical adoption. Applying a B_1 correction map is 1 technique, among others, that can be used to compensate for the inhomogeneities in the transmit field. In this study, we showed that B_1 correction using the Bloch–Siegert shift is a viable (and attractive) option to measure accurate and precise VFA-derived T_1 values in the breast at 3 T.

Supplemental Materials

Supplemental Figure 1: http://dx.doi.org/10.18383/j.tom.2016.00133.sup.01

Supplemental Figure 2: http://dx.doi.org/10.18383/j.tom.2016.00133.sup.02

Supplemental Figure 3: http://dx.doi.org/10.18383/j.tom.2016.00133.sup.03

Supplemental Table 1: http://dx.doi.org/10.18383/j.tom.2016.00133.sup.04

Supplemental Table 2: http://dx.doi.org/10.18383/j.tom.2016.00133.sup.05

Supplemental Table 3: http://dx.doi.org/10.18383/j.tom.2016.00133.sup.06

ACKNOWLEDGMENTS

We thank the National Institutes of Health for funding through NCI 1R01CA129961, NCI 1U01CA142565, NCI 1P50 098131, NIH P30 CA68485, and NIBIB K25 EB013659. We offer our sincere thanks to the women who participated in our study. We would also like to thank Dr. Jeffrey J. Luci for informative discussions on the technical aspects of the Bloch–Siegert sequence, and Ms. Leslie McIntosh and Ms. Kristen George-Durrett for providing expert MRI system-specific technical assistance.

Disclosures: No disclosures to report.

Conflict of Interest: None reported.

REFERENCES

1. Petrillo M, Fusco R, Catalano O, Sansone M, Avallone A, Delrio P, Pecori B, Tatangelo F, Petrillo A. MRI for assessing response to neoadjuvant therapy in locally advanced rectal cancer using DCE-MR and DW-MR data sets: a preliminary report. Biomed Res Int. 2015;2015:514740.
2. Piludu F, Marzi S, Pace A, Villani V, Fabi A, Carapella CM, Terrenato I, Antenucci A, Vidiri A. Early biomarkers from dynamic contrast-enhanced magnetic resonance imaging to predict the response to antiangiogenic therapy in high-grade gliomas. Neuroradiology. 2015;57(12):1269–1280.
3. Chawla S, Kim S, Dougherty L, Wang S, Loevner LA, Quon H, Poptani H. Pretreatment diffusion-weighted and dynamic contrast-enhanced MRI for prediction of local treatment response in squamous cell carcinomas of the head and neck. AJR Am J Roentgenol. 2013;200(1):35–43.
4. Abramson RG, Li X, Hoyt TL, Su PF, Arlinghaus LR, Wilson KJ, Abramson VG, Chakravarthy AB, Yankeelov TE. Early assessment of breast cancer response to neoadjuvant chemotherapy by semi-quantitative analysis of high-temporal resolution DCE-MRI: preliminary results. Magn Reson Imaging. 2013;31(9):1457–1464.
5. Li X, Arlinghaus LR, Ayers GD, Chakravarthy AB, Abramson RG, Abramson VG, Atuegwu N, Farley J, Mayer IA, Kelley MC, Meszoely IM, Means-Powell J, Grau AM, Sanders M, Bhave SR, Yankeelov TE. DCE-MRI analysis methods for predicting the response of breast cancer to neoadjuvant chemotherapy: pilot study findings. Magn Reson Med. 2014;71(4):1592–1602.
6. Yankeelov TE, Gore JC. Dynamic contrast enhanced magnetic resonance imaging in oncology: theory, data acquisition, analysis, and examples. Curr Med Imaging Rev. 2009;3(2):91–107.
7. Brookes JA, Redpath TW, Gilbert FJ, Murray AD, Staff RT. Accuracy of T1 measurement in dynamic contrast-enhanced breast MRI using two- and three-dimensional variable flip angle fast low-angle shot. J Magn Reson Imaging. 1999;9(2):163–171.
8. Wang HZ, Riederer SJ, Lee JN. Optimizing the precision in T1 relaxation estimation using limited flip angles. Magn Reson Med. 1987;5(5):399–416.
9. Yankeelov TE, Pickens DR, Price RR. Quantitative MRI in Cancer. Hendee WR, editor. Boca Raton, Florida: Taylor & Francis Group, LLC, 2012.
10. Tofts PS, Berkowitz B, Schnall MD. Quantitative analysis of dynamic Gd-DTPA enhancement in breast tumors using a permeability model. Magn Reson Med. 1995;33(4):564–568.
11. Di Giovanni P, Azlan CA, Ahearn TS, Semple SI, Gilbert FJ, Redpath TW. The accuracy of pharmacokinetic parameter measurement in DCE-MRI of the breast at 3 T. Phys Med Biol. 2010;55(1):121–132.
12. Cunningham CH, Pauly JM, Nayak KS. Saturated double-angle method for rapid B1+ mapping. Magn Reson Med. 2006;55(6):1326–1333.
13. Cohen MS, DuBois RM, Zeineh MM. Rapid and effective correction of RF inhomogeneity for high field magnetic resonance imaging. Hum Brain Mapp. 2000;10(4):204–211.
14. Kuhl CK, Kooijman H, Gieseke J, Schild HH. Effect of B1 inhomogeneity on breast MR imaging at 3.0 T. Radiology. 2007;244(3):929–930.
15. Azlan CA, Di Giovanni P, Ahearn TS, Semple SI, Gilbert FJ, Redpath TW. B1 transmission-field inhomogeneity and enhancement ratio errors in dynamic contrast-enhanced MRI (DCE-MRI) of the breast at 3T. J Magn Reson Imaging. 2010;31(1):234–239.
16. Pineda FD, Medved M, Fan X, Karczmar GS. B1 and T1 mapping of the breast with a reference tissue method. Magn Reson Med. 2015;75(4):1565–1573.
17. Sung K, Saranathan M, Daniel BL, Hargreaves BA. Simultaneous T(1) and B(1)(+) mapping using reference region variable flip angle imaging. Magn Reson Med. 2013;70(4):954–961.
18. Kuhl CK, Jost P, Morakkabati N, Zivanovic O, Schild HH, Gieseke J. Contrast-enhanced MR imaging of the breast at 3.0 and 1.5 T in the same patients: initial experience. Radiology. 2006;239(3):666–676.
19. Hornak JP, Szumowski J, Bryant RG. Magnetic field mapping. Magn Reson Med. 1988;6(2):158–163.
20. Yarnykh VL. Actual flip-angle imaging in the pulsed steady state: a method for rapid three-dimensional mapping of the transmitted radiofrequency field. Magn Reson Med. 2007;57(1):192–200.
21. Morrell GR. A phase-sensitive method of flip angle mapping. Magn Reson Med. 2008;60(4):889–894.
22. Jiru F, Klose U. Fast 3D radiofrequency field mapping using echo-planar imaging. Magn Reson Med. 2006;56(6):1375–1379.
23. Duan Q, van Gelderen P, Duyn J. Improved Bloch-Siegert based B1 mapping by reducing off-resonance shift. NMR Biomed. 2013;26(9):1070–1078.
24. Sacolick LI, Wiesinger F, Hancu I, Vogel MW. B1 mapping by Bloch-Siegert shift. Magn Reson Med. 2010;63(5):1315–1322.

25. Jankiewicz M, Gore JC, Grissom WA. Improved encoding pulses for Bloch-Siegert B1(+) mapping. J Magn Reson. 2013;226:79–87.
26. Park DJ, Bangerter NK, Javed A, Kaggie J, Khalighi MM, Morrell GR. A statistical analysis of the Bloch-Siegert B1 mapping technique. Phys Med Biol. 2013; 58(16):5673–5691.
27. Bloch F, Siegert A. Magnetic resonance for nonrotating fields. Phys Rev. 1940; 57(6):522–527.
28. Steffen M, Vandersypen LM, Chuang IL. Simultaneous soft pulses applied at nearby frequencies. J Magn Reson. 2000;146(2):369–374.
29. Li X, Abramson RG, Arlinghaus LR, Kang H, Chakravarthy AB, Abramson VG, Farley J, Mayer IA, Kelley MC, Meszoely IM, Means-Powell J, Grau AM, Sanders M, Yankeelov TE. Multiparametric magnetic resonance imaging for predicting pathological response after the first cycle of neoadjuvant chemotherapy in breast cancer. Invest Radiol. 2015;50(4):195–204.
30. Li K, Zu Z, Xu J, Janve VA, Gore JC, Does MD, Gochberg DF. Optimized inversion recovery sequences for quantitative T1 and magnetization transfer imaging. Magn Reson Med. 2010;64(2):491–500.
31. Efron B. Bootstrap methods: another look at the jackknife. Ann Stat. 1979;7(1):1–26.
32. Bland JM, Altman DG. Measuring agreement in method comparison studies. Stat Methods Med Res. 1999;8(2):135–160.
33. Dula AN, Arlinghaus LR, Dortch RD, Dewey BE, Whisenant JG, Ayers GD, Yankeelov TE, Smith SA. Amide proton transfer imaging of the breast at 3 T: establishing reproducibility and possible feasibility assessing chemotherapy response. Magn Reson Med. 2013;70(1):216–224.
34. Zhu H, Arlinghaus LR, Whisenant JG, Li M, Gore JC, Yankeelov TE. Sequence design and evaluation of the reproducibility of water-selective diffusion-weighted imaging of the breast at 3 T. NMR Biomed. 2014;27(9): 1030–1036.
35. Sung K, Daniel BL, Hargreaves BA. Transmit B1+ field inhomogeneity and T1 estimation errors in breast DCE-MRI at 3 tesla. J Magn Reson Imaging. 2013; 38(2):454–459.
36. Bedair R, Graves MJ, Patterson AJ, McLean MA, Manavaki R, Wallace T, Reid S, Mendichovszky I, Griffiths J, Gilbert FJ. Effect of radiofrequency transmit field correction on quantitative dynamic contrast-enhanced MR imaging of the breast at 3.0 T. Radiology. 2015;279(2):150920.
37. Ma J. Breath-hold water and fat imaging using a dual-echo two-point Dixon technique with an efficient and robust phase-correction algorithm. Magn Reson Med. 2004;52(2):415–419.
38. Nehrke K, Börnert P. DREAM–a novel approach for robust, ultrafast, multislice B(1) mapping. Magn Reson Med. 2012;68(5):1517–1526.
39. Li X, Dawant BM, Welch EB, Chakravarthy AB, Freehardt D, Mayer I, Kelley M, Meszoely I, Gore JC, Yankeelov TE. A nonrigid registration algorithm for longitudinal breast MR images and the analysis of breast tumor response. Magn Reson Imaging. 2009;27(9):1258–1270.